Research article

Facile fabrication of ZnO nanoparticles via non-thermal plasma technique and their anti-corrosive effects on X60 API 5L steel in 1M HCl solution

Nourelhouda Bounedjar [a,b,**], Mohammed Fouad Ferhat [a,c,d], Chun Ouyang [e], Mohamed Bououdina [f], Ihab Shawish [f], Rasha A. Abumousa [f], Muhammad Humayun [f,*]

[a] Renewable Energy Development Unit in Arid Zones (UDERZA), University of El Oued, 39000, El Oued, Algeria
[b] Department of Chemistry, Faculty of Exact Sciences, University of El Oued, B.P. 789, 39000, Algeria
[c] Laboratory of Sciences and Techniques of the Environment and Valuation, Ibn Badis-Mostaganem University, Algeria
[d] Department of Process Engineering, Faculty of Technology, University of El Oued, B.P. 789, 39000, Algeria
[e] School of Materials Science and Engineering, Jiangsu University of Science and Technology, Zhenjiang, 212003, Jiangsu Province, China
[f] Energy, Water and Environment Lab, College of Humanities and Sciences, Prince Sultan University, Riyadh, 11586, Saudi Arabia

ARTICLE INFO

ABSTRACT

This work aims to explore the efficiency of ZnO nanoparticles synthesized via the non-thermal gliding arc discharge-assisted plasma (NT-GAD) technique for inhibiting the corrosion of X60 API 5L steel in a 1M HCl environment. The XRD pattern revealed that the ZnO nanoparticles exhibit hexagonal wurtzite structure with average particle size of ~24 nm. UV–visible spectroscopy analysis revealed an absorption peak centering at 365 nm, corresponding to an energy band gap of 3.29 eV. SEM and TEM analysis revealed that the nanoparticles exhibit an agglomerated and irregular morphology. The corrosion inhibition of ZnO NPs was investigated via the electrochemical impedance spectroscopy (EIS) and potentiodynamic polarization tests (PDP), while varying both concentration and temperature. The results revealed that the increase in inhibitor concentration resulted in a higher activity at ambient temperature, with an optimal efficiency of 93 % at a concentration of 100 mg/L. However, the increase in temperature remarkably reduced the inhibition efficiency, suggesting a physisorption behavior of ZnO NPs onto the steel surface. AFM and FE-SEM analysis confirmed the formation of a protective layer on the X60 API 5L steel surface. This study emphasizes the significant potential of ZnO NPs synthesized via the NT-GAD assisted plasma technique as corrosion inhibitor for X60 API 5L carbon steel in 1M HCl corrosive media.

1. Introduction

The transportation of oil and natural gas using pipelines plays an essential role in the energy industry. It enables the movement of these economical resources from extraction sites at drill stations to treatment centers, through pumping stations, compressor stations,

* Corresponding author.
** Corresponding author. Renewable Energy Development Unit in Arid Zones (UDERZA), University of El Oued, 39000, El Oued, Algeria.
E-mail addresses: nourelhouda-bounedjar@univ-eloued.dz (N. Bounedjar), mhumayun@psu.edu.sa (M. Humayun).

Table 1
The chemical composition of the X60 API5L substrate.

Elements	C	P	S	Cr	Mn	Ni	Al	Cu	Sn	V	Mo	Si	Ti	Co	W	Fe
Value % ($\times 10^{-3}$)	1800	10.2	3.1	82.4	1200	98.2	18.3	18.6	3.1	57	93	36.4	<1	13	15	rest

and storage tanks. This ensures easy transportation from hydrocarbon treatment facilities to national and international markets [1]. The construction of oil and gas pipelines, along with treatment facilities and storage equipment, mostly relies on the utilization of carbon steel and its variants. This preference is attributed to their great mechanical properties, low cost, and widespread availability, rendering them suitable for deployment in both soil and underwater environments [2]. Consequently, within the oil and gas industry, ensuring the safety of these pipelines, equipment, and facilities emerges as a vital concern, aiming to extend their operational lifespan and enhance durability. Despite regular maintenance, these materials remain vulnerable to wear and damage over time, primarily due to corrosion. In order to retard and mitigate corrosion and prolong the lifespan of this equipment's and pipelines, the use of corrosion inhibitors becomes inevitable. Corrosion inhibitors work by changing the metallic surface through the adsorption of inhibitor molecules, creating a barrier between the metal and corrosive agents These molecules attach to the metal surface in a manner specific to their nature. Metal oxide inhibitors are commonly tested at concentrations ranging from 50 to 200 ppm in an electrolyte. The steel usually gets tested in the presence of HCl to establish the link between the Cl^- concentration in the electrolyte and the appropriate inhibitor concentration required to prevent steel corrosion [3].

Lately, research has been directed toward the use of sustainable materials for corrosion mitigation. For this reason, metal oxide nanoparticles have grabbed attention owing to their potential for wide application across various fields, such as energy [4], photo-catalysis [5], biomedicine [6], agriculture [7], and corrosion inhibition [8]. Numerous researchers have reported a variety of studies showing good results regarding the use of ZnO NPs as a protective method against corrosion [9,10]. However, the investigation of ZnO NPs fabricated via the non-thermal plasma technique and annealed at 773 K for the purpose of inhibiting X60 API 5L steel has not been reported so far.

In the last few decades, various techniques have been reported for the synthesis of ZnO NPs, each showing different yields and scalability [11–14]. These techniques include the sol-gel [15], energy ball milling [16], gas-phase conversion [17], ultrasound-assisted [18], chemical vapor deposition [19], electrodeposition [20], and green synthesis method [21]. However, majority of these techniques have certain limitations, such as low product yield, time-consuming procedures, the presence of toxic impurities due to the utilization of chemical reagents during the synthesis process, and high production costs. To overcome these challenges, a novel synthesis approach has been developed, offering advantages that surpass those associated with the previously mentioned techniques. This method utilizes non-thermal plasma (NTP), particularly the Gliding Arc Discharge-assisted (GAD) technique, for the synthesis of ZnO nanoparticles.

The primary aim of this research is to synthesize ZnO NPs using non-thermal plasma technique to mitigate corrosion in X60 API 5L carbon steel exposed to a 1M HCl medium. To confirm the success of the synthesis protocol, the optical, morphological, and structural properties of the NPs were explored through UV–visible (UV–vis), Fourier Transform Infrared (FT-IR), X-ray Diffraction (XRD), Scanning Electron Microscopy (SEM), and Energy Dispersive X-ray Spectroscopy (EDX), Transmission Electron Microscopy (TEM) and X-ray Photoelectron Spectroscopy (XPS) techniques. Furthermore, the inhibition efficiency of ZnO NPs for X60 AP I5L carbon steel in the 1M HCl solution was assessed through electrochemical studies, varying two key parameters: i.e., concentration and temperature. Additionally, Atomic Force Microscopy (AFM) and Field Emission Scanning Electron Microscopy (FE-SEM) were employed to analyze the substrate's surface morphology and the adsorption mechanism of the ZnO NPs film on X60 API 5L steel. This study confirms that ZnO NPs can serve as an effective corrosion inhibitor for X60 API 5L in the 1M HCl medium.

2. Experimental section

2.1. Materials and chemicals

Zinc acetate dihydrate (Zn (CH$_3$O$_2$)$_2$·2H$_2$O) and 37 % analytical grade HCl were purchased from Sigma Aldrich Chemicals (Missouri, USA), and the products were used without further purification. The aggressive stock solution of 1 M HCl medium was prepared by dilution with distilled water, and the working solutions were prepared by dissolving ZnO NPs in a known volume of the medium to obtain concentrations of 0, 20, 40, 60, 80, and 100 mg/L.

2.2. Substrate preparation

X60 API 5L steel was used as the working electrode for the corrosion inhibition tests. The chemical composition of the substrate is mentioned in Table 1 [22,23]. The substrate had dimensions of 1×1 cm^2 and was cut using a machine equipped with a cooling fluid system to minimize mechanical damage during the cutting procedure. Afterward, it was connected to a copper wire before being covered with resin to leave a 1 cm^2 surface of the substrate exposed to the acidic medium. The substrate surface was polished using a series of SiC papers of different grades (400–2000), then finished with diamond paste in order to obtain a mirror surface, rinsed with distilled water, and then washed with ethanol and degreased using 70 % acetone. Finally, it was rinsed again with distilled water and dried under a flow of air for the final preparation prior to each test.
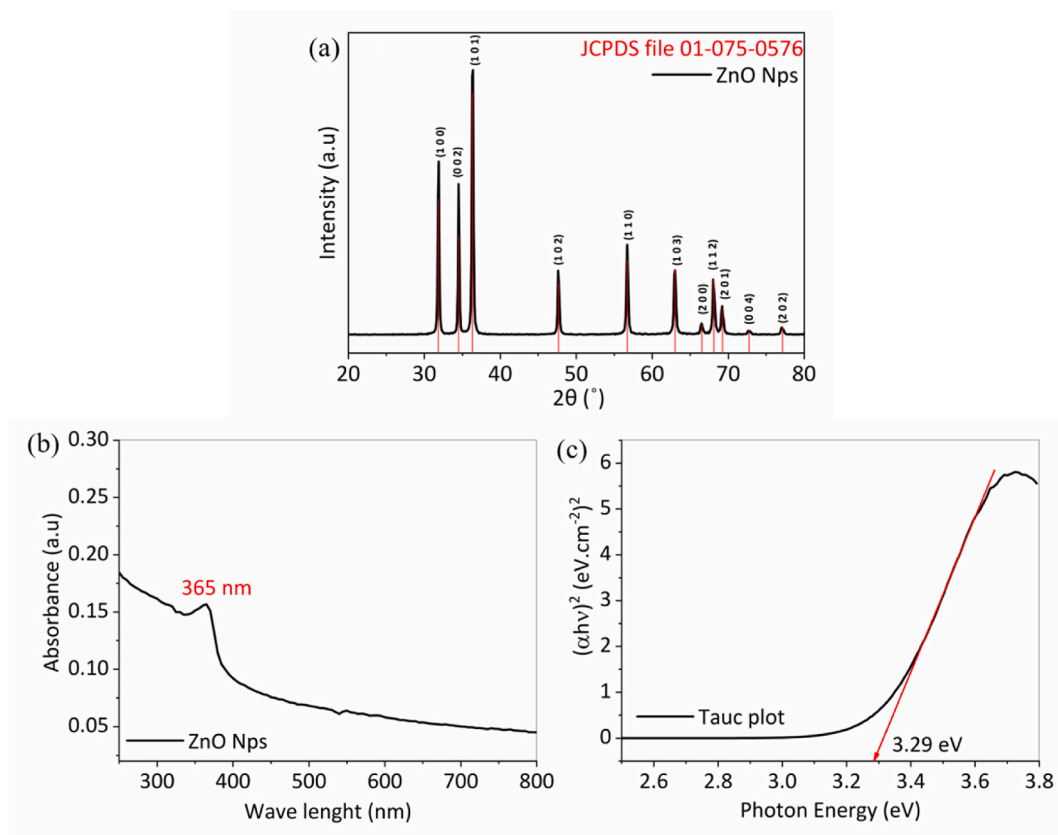
Fig. 1. (a) XRD pattern, (b) UV–vis absorption spectrum, and (c) Tauc's plot of ZnO NPs synthesized via the nonthermal plasma technique and annealed at 773K.

2.3. Synthesis of ZnO nanoparticles

The GAD reactor used for the synthesis of ZnO NPs comprise of symmetric pair of 304L SS electrodes connected to a high-voltage transformer that delivered a 9 KV current, along with a compressor that supplied 16 L/min of humid air saturated with water as the feeding gas [24,25]. This synthesis method was chosen for its ability to yield nanoparticles with high purity and its efficiency in preventing the generation of harmful byproducts. Approximately, 2g of zinc acetate dehydrate was taken as a precursor for nanoparticle synthesis due to its stability and high-water solubility. The precursor was placed in 100 ml of distilled water and stirred for 10 min at room temperature until complete dissolution was achieved. The feeding gas nozzle and the GAD reactor electrodes were positioned at 5 cm above the designated solution while continuously stirred under atmospheric pressure for 15 min exposure to the plasma discharge. Afterward, the GAD discharge was turned off, and the resulting cloudy solution was dried on a hotplate at 100 °C (373.15 K), and then annealed at 500 °C (773.15 K) for 4 h. This process was repeated multiple times, and the resulting ZnO NPs were then ground into fine powder.

2.4. Characterization

Several methods were employed to characterize the structure, chemical composition, size, optical properties, and crystallography of the as-prepared ZnO nanoparticles. The crystalline nature and phase of ZnO NPs were examined using the X-ray Bruker Diffractometer Bruker D8 Advance target, alongside copper Kα1 and a monochromator ($\lambda = 1.5405$ Å) at 40 kV and 40 mA. The NPs were prepared and analyzed according to earlier study. The UV–vis absorption spectrum of the prepared ZnO NPs in a 1 M HCl solvent was taken in a 1 cm thick quartz cell through a UNICAM UV 300 spectrophotometer (Made in USA). Electronic spectra were plotted in the wavelength range between 250 and 800 nm. The morphology of the ZnO NPs was studied with scanning electron microscopy (SEM) using a ZEISS EVO 15 microscope Germany, coupled with an X-ray spectrometer energy dispersive (EDX) using a 6490 LA detector. The EDX analysis included both EDS mapping and EDX spectrum along with the atomic% and weight% composition of Zn and O elements in the ZnO NPs. The elemental chemical states of the ZnO NPs were investigated via the XPS (thermos-ESCALAB-250XI, USA) equipment. Adventitious carbon contamination with binding energy of 284.4 eV was used as a charge reference for the measurement of XPS spectra. The surface morphology of API 5L X60 was examined using field emission scanning electron microscopy (FE-SEM) using the SEM-TM1000 Hitachi Model and atomic force microscopy (AFM) with Bruker's Dimension Icon. The investigation aimed to
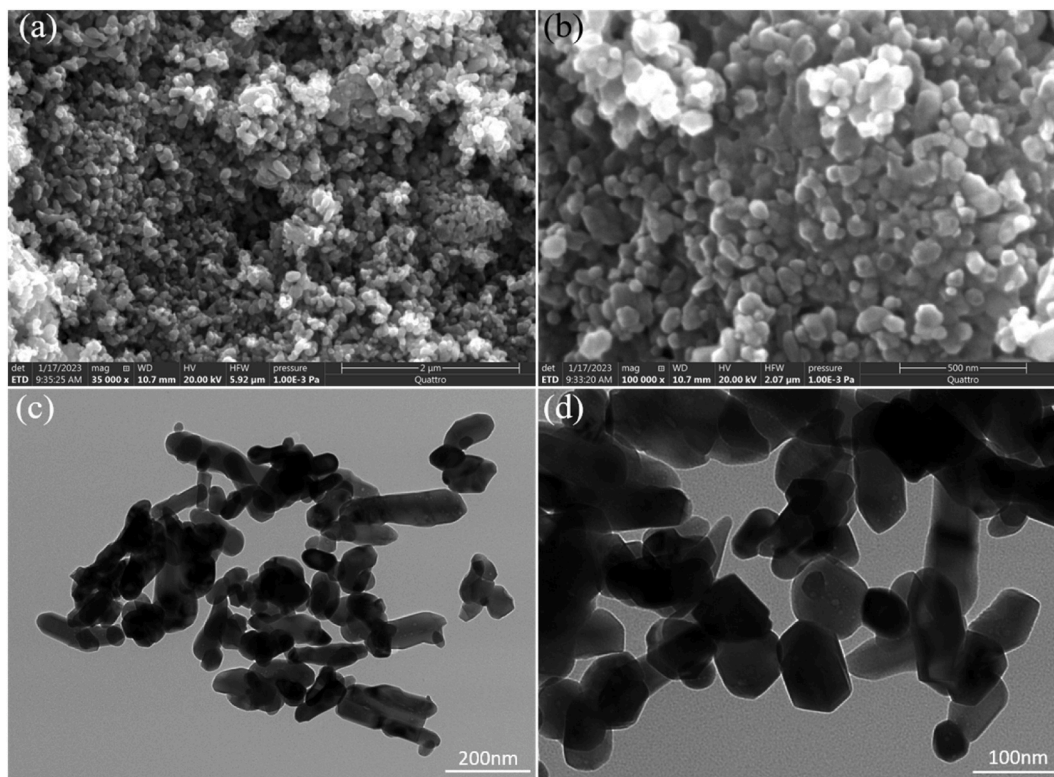
Fig. 2. (a, b) SEM micrographs, and (c, d) TEM images of ZnO NPs.

observe the film formation and to understand the surface behavior of the substrate after immersion in 1M HCl, for both uninhibited and inhibited with an effective concentration of 100 mg/L of ZnO NPs. The immersion times for evaluation were 24 h and 5 h in the aggressive media, respectively. The substrates were prepared following the protocol outlined in the substrate preparation section.

2.5. Electrochemical measurements

The inhibitory effects of ZnO nanoparticles on the corrosion of API 5L X60 carbon steel in 1M HCl medium were evaluated using an electrochemical Pyrex cell with a volume of 50 cm^3, which had a three-electrode setup. An Ag/AgCl saturated KCl served as a reference electrode, a 2 cm^2 platinum plate as a counter electrode, and a 1×1 cm^2 square shaped plate of API 5L X60 steel surface covered with resin as the working electrode. The electrochemical analysis and polarization corrosion tests were assessed under 1 M HCl solution, with two crucial parameters being varied: (i) the inhibitor's concentration and (ii) the temperature.

- (i) Concentration effect of ZnO NPs inhibitor was investigated by immersing them in solutions with concentrations ranging from 0 to 100 mg/L at room temperature for a duration of 60 min.
- (ii) Temperature effect was investigated at various temperatures (i.e., 298, 303, 313, 323, and 333 K) using a water bath with a thermostat. The experiments were conducted using the optimal concentration of 100 mg/L of ZnO NPs.

The experiments were conducted using an Interface Volta Lab PGZ301, France, piloted with Volta master 4 analysis software. A potential scan rate for polarization corrosion tests (PDP) was 1 mV/s and an impedance frequency for electrochemical impedance spectra (EIS) ranged from 100 kHz to 10 mHz, and a signal amplitude perturbation of 10 mV, to determine the corrosion rate and inhibition efficiency.

3. Results and discussion

3.1. Structural characterization and chemical composition

X-ray diffraction analysis was performed to explore the characteristic diffraction peaks of ZnO NPs synthesized via the non-thermal plasma technique. Fig. 1a reveals distinct peaks at *2θ* values of 31.86°, 34.54°, and 36.36°, indicating hexagonal wurtzite structure of the as-prepared ZnO NPs. Additionally, other peaks are observed at *2θ* values of 47.66°, 56.71°, 62.99°, 66.48°, 68.08°, 69.22°, 72.72°, and 77.09°, corresponding to the (100), (002), (101), (102), (110), (103), (200), (112), (201), (004), and (202) crystallographic planes
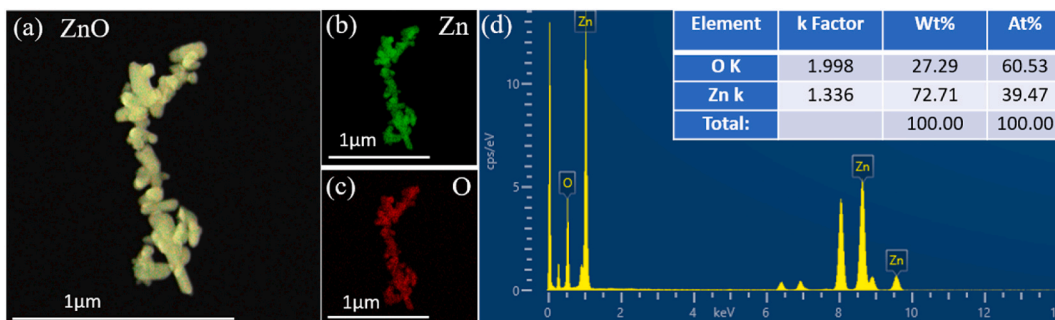
Fig. 3. (a–c) EDS elemental mapping, and (d) Energy Dispersive X-ray spectrum of ZnO NPs.
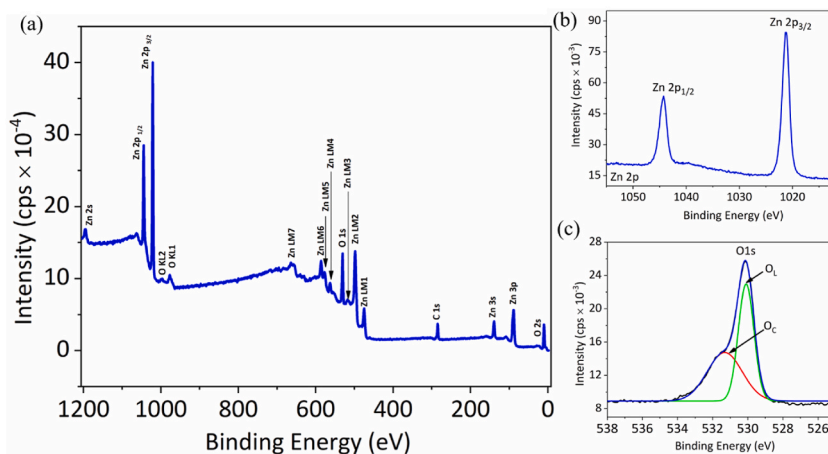

Fig. 4. (a) XPS survey spectrum, (b) high resolution Zn2p XPS, and (c) high resolution O1s XPS of ZnO NPs annealed at 773K.

of ZnO NPs, respectively. This confirms the polycrystalline nature of the sample [26]. These values are in good agreement with the data recorded in the JCPDS file 01-075-0576. The crystallite size (D) was determined through the Debye-Scherer equation [27]. In this equation, "λ" represents the wavelength (1.54060 Å), "K" represents the Debye-Scherer's constant (K ≈ 0.91), "θ" is the Bragg's angle at which the (101) peak was observed, "β" is the peak full width at half maximum (in radians), and "D" is the average crystallite size. From XRD pattern, the crystallite size of ZnO NPs was calculated to be 24.41 nm. Consequently, the decrease in crystallite size indirectly results in an increase in the specific surface area, which holds great potential in corrosion mitigation application [28]. Furthermore, the presence of intense and sharp peak shapes, along with the absence of any impurity peaks confirms that the as-prepared ZnO NPs are of fine grade and high purity [29]. This observation can be attributed to the exclusion of any chemical solvent during the synthesis process.

Fig. 1b depicts the UV–visible absorption spectrum of the as-prepared ZnO NPs recorded in the wavelength range of 250–800 nm. The ZnO NPs shows an absorption peak centering at 365 nm, corresponding to the energy band gap of 3.29 eV, according to the widely accepted energy band gap equation: $E_g = 1240/\lambda$. The optical band gap energy of the as-synthesized ZnO NPs was further confirmed by extrapolating the linear portion of the Tauc plot of $(\alpha h\upsilon)^2$ versus ($h\upsilon$) according to the Tauc equation (equation (1)) as follows [30]:

$$(\alpha h\upsilon)^2 = D (h\upsilon - E_g) \tag{1}$$

In the above equation, "E_g" is the optical band gap of the sample, "$h\upsilon$" is the incident photon energy, "D" is a constant, and "α" is the absorption coefficient constant.

Fig. 1c illustrates the Tauc plot of ZnO NPs. As obvious, the NPs exhibit an energy band gap of 3.29 eV. This value suggests that ZnO NPs possess a relatively wide band gap, reflecting their good optical and electronic properties. The observed band gap falls within the reported band gap range of 3.10–3.37 eV for bulk ZnO [31]. The obtained value of the band gap for ZnO NPs can be attributed to multiple factors, such as particle size, the presence of vacancies, and the crystalline structure [32].

Fig. 2a, b illustrates the SEM micrographs of the as-prepared ZnO NPs. It can be seen clearly that the ZnO NPs display a spherical morphology with average particles size in the range of 20–30 nm. Notably, the nanocrystalline particles are agglomerated. Furthermore, these nanoparticles exhibit notable porosity [33]. The morphological structure of ZnO NPs was further investigated via the Transmission Electron Microscopy (TEM) technique. The TEM images of ZnO NPs (Fig. 2c and d) reveal polymorphic nature. Further, the nanoparticles tend to agglomerate, showing various sizes and shapes. The nanoparticles reveal different morphologies appearing in
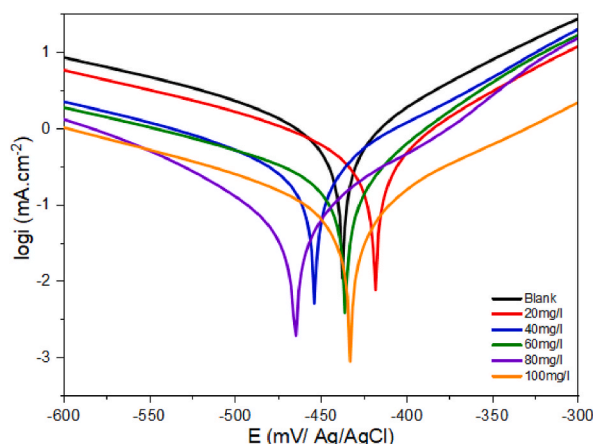
Fig. 5. Tafel plots of API 5L X60 in an uninhibited 1M HCl solution and inhibited with various concentrations of ZnO NPs.

Table 2
Polarization parameters for X60 API 5L in an uninhibited 1M HCl solution and when inhibited with various concentrations of ZnO NPs.

C(mg/L)	E $_{corr}$	i $_{corr}$ (mA.cm^{-2})	β_a (mV·dec^{-1})	$-\beta_c$ (mV·dec^{-1})	θ	EI%
Blank	436.1	2.40	82.2	87.7	/	/
20	418.4	0.42	93.4	98.7	0.8232	82.32
40	424.2	0.36	58.1	92.9	0.8472	84.72
60	485.4	0.26	76.2	86.6	0.8914	89.14
80	447.4	0.21	83.5	110.7	0.9124	91.24
100	432.7	0.15	99.7	89.6	0.9350	93.50

near-spheroids, elongated rods, hexagonal prisms, and polyhedral forms. This variation in the shape and size of ZnO nanoparticles is attributed to the used synthesis method [34]. The gradual release of highly reactive hydroxyl radical ($^{\bullet}$OH) during the plasma reaction and their interaction with the target solution is found to promote the aggregation of the ZnO NPs [35].

Fig. 3a–c reveals the EDS elemental mappings of the ZnO NPs. As obvious, the Zn and O elements are uniformly distributed in the ZnO NPs. Furthermore, the EDX spectrum of ZnO NPs (Fig. 3d) clearly indicate that the weight percentage of oxygen (O) and zinc (Zn) in the as-prepared ZnO NPs is 27.29 and 72.71 %, respectively. As obvious, no impurity peaks can be observed in the EDX spectrum of ZnO NPs, further validating its high purity [36].

Fig. 4(a–c) present the XPS spectra of ZnO NPs synthesized via nonthermal plasma technique. The XPS survey spectrum of ZnO NPs (Fig. 4a) confirms the presence of only zinc and oxygen elements. Fig. 4b reveals two distinct and symmetric peaks within the Zn 2p spectrum, at binding energies of 1044.34 eV (Zn 2p$_{1/2}$) and 1021.2 eV (Zn 2p$_{3/2}$), indicating the 2+ oxidation state of Zn in the ZnO NPs [37]. Fig. 4c reveals the deconvoluted O 1s spectrum with two Gaussian components at 530.07 and 531.27 eV, which can be attributed to chemisorbed oxygen species and lattice oxygen within the wurtzite structure of hexagonal ZnO, respectively [38]. These findings demonstrate that the chemical structure of ZnO NPs is predominantly comprised of zinc in the (+2) oxidation state and oxygen in the form of O^{2-}. This confirms the high quality and purity of the ZnO NPs, and validating that the nonthermal plasma synthesis technique is a promising method for producing ZnO NPs with minimal impurities and defects.

3.2. Corrosion kinetics study

3.2.1. Polarization of concentration effect

Fig. 5 depicts the polarization plots obtained for X60 API-5L steel in an uninhibited 1M HCl solution and inhibited with various concentrations of ZnO NPs, which were tested at 298K (24.85 °C). The corrosion measurement parameters, including corrosion potential (E_{corr}), cathodic and anodic Tafel slopes (β_c and β_a), recovery rate (θ), inhibition efficiency (EI %), and corrosion current densities (i_{corr}) are summarized in Table 2.

The recovery rate and inhibition efficiency were determined for different concentrations of ZnO NPs in 1M HCl as expressed by equation (2) [39,40] and equation (3) [12]:

$$\theta = (i_{corr} - i_{corr\,(inh)}/i_{corr}) \tag{2}$$

$$EI\ (\%) = \theta \times 100 \tag{3}$$

In equation (2), i_{corr} and $i_{corr\,(inh)}$ represents the values of the substrate corrosion current density obtained by analyzing the Tafel plots in an uninhibited 1M HCl solution and inhibited with different concentrations of ZnO NPs, respectively.
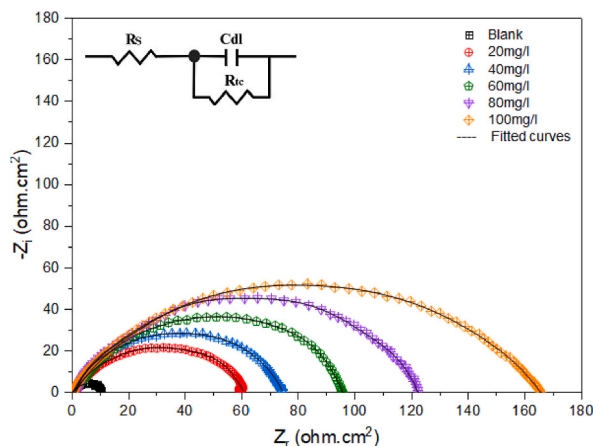
Fig. 6. EIS Nyquist curves for X60 API 5L steel uninhibited 1M HCl and inhibited with various concentration of ZnO NPs at 298K, (insert: Electrical Circuit used to Model the Impedance Diagram).

Table 3
EIS parameters data X60 API 5L steel uninhibited 1M HCl and inhibited with ZnO NPs in various concentrations at 298K.

C (mg/L)	Rs ($\Omega \cdot cm^{-2}$)	Rct ($\Omega \cdot cm^{-2}$)	C_{dl} (mF$\cdot$cm^{-2})	θ	EI (%)
Blank	0.88	10.48	1.51	/	/
20	0.62	60.63	0.23	0.8271	82.71
40	0.55	74.56	0.24	0.8594	85.94
60	0.39	100.6	0.18	0.8958	89.58
80	0.24	121.0	0.16	0.9133	91.33
100	0.19	165.3	0.06	0.9366	93.66

As obvious, the addition of ZnO NPs had an impact on the two partial corrosion reactions, resulting in a decrease in both the cathodic and anodic current densities. Additionally, there was a slight displacement of the E_{corr}. These findings suggest that the inhibition process occurs through the adsorption of ZnO NPs on the steel surface, indicating that ZnO NPs influence the kinetics of hydrogen reduction and metal dissolution.

Table 2 illustrates that the introduction of ZnO NPs results in irregular changes in the anodic (βa) and cathodic (βc) Tafel slopes. Both βa and βc exhibit similar patterns of change, which suggests that ZnO NPs function as an effective mixed-type inhibitor, influencing both anodic and cathodic reactions. Additionally, the corrosion current densities (i_{corr}) for the inhibited solutions are significantly lower compared to the uninhibited solution. This reduction in i_{corr} indicates a higher surface coverage (θ), achieved by the ZnO NPs blocking the active sites on the carbon steel surface, thereby reducing the overall corrosion rate. These observations indicate that the inhibitor displays an increasing inhibitory efficiency (EI%) at higher concentrations, reaching an optimum value of 93.50 % with a concentration of 100 mg/L. Consequently, these findings confirm the efficiency of ZnO NPs in inhibiting the corrosion of X60 API 5L steel in a 1M HCl solution.

3.2.2. EIS study of concentration effect

Fig. 6 depicts the EIS response of X60 API 5L steel in 1M HCl, both uninhibited and inhibited with varying concentrations of ZnO NPs. Analysis of the EIS Nyquist plots reveals a semi-circular shape that increases in diameter as the concentration of ZnO NPs increases. This phenomenon can be attributed to the accelerated inhibition rate on the carbon steel surface, effectively retarding the corrosion process. Moreover, adding ZnO NPs at varying concentrations does not alter the shape of the impedance curves, indicating that the mechanism by which ZnO NPs inhibit corrosion remains consistent across different concentrations. The imperfect semi-circles are often associated with frequency dispersion caused by the rigidity or irregularity of the metal surface. The observed plots are represented in the real part (Z') and imaginary part (Z'') of the EIS Nyquist plot [41].

Table 3 shows the corrosion parameters such as the capacity of the double layer (C_{dl}) and the charge transfer resistance (R_{ct}) determined at low and high frequencies, and the inhibition efficacy was calculated using equation (4) as follows [42]:

$$EI\ (\%) = (Rct_{inh} - Rct_{blank})/Rct_{inh} \times 100 \tag{4}$$

Where, $R_{ct(blank)}$ and $R_{ct(inh)}$ are the values of X60 API 5L charge transfer resistance for the uninhibited 1M HCl solution and inhibited with ZnO NPs, respectively. The C_{dl} values were calculated using equation (5) as follows [43]:

$$C_{dl} = 1/[2\pi f(-Zmax)] \times Rct \tag{5}$$

Where, f is the frequency on the EIS Nyquist plot when the imaginary value reaches its maximum. Several kinetic models of equivalent
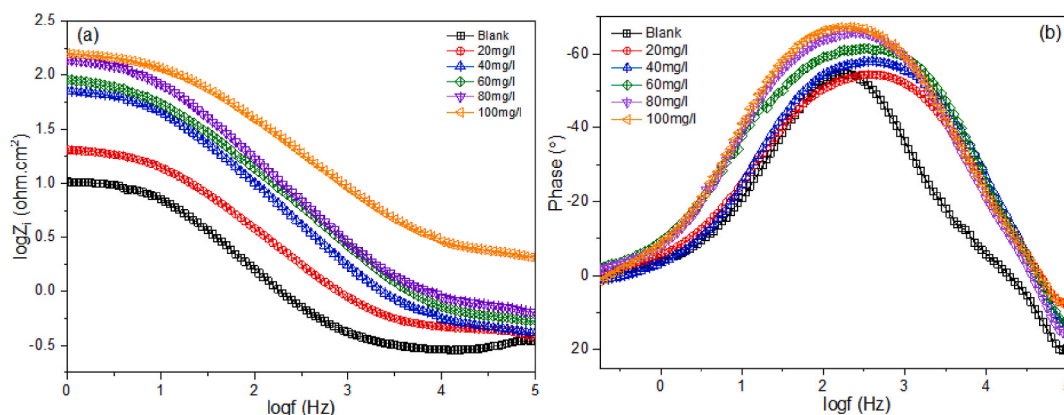
Fig. 7. (a) Bode diagram, and (b) phase angle curves of corrosion of X60 API5L steel in 1M HCl with different concentration of the ZnO NPs at 298 K.

electrical circuits were tested in order to determine the most relevant to simulate the behavior of the interface of the studied systems. Most of the results obtained were unsatisfactory. After several attempts, the best fits have a correlation coefficient $\chi^2 = 0.95211$ using the equivalent electrical circuit.

Fig. 7a, b shows the Bode diagram and the phase angle, respectively. Fig. 7a indicates the presence of an equivalent circuit that contains a single-phase element constant between the metal and solution interface for X60 API 5L steel in 1M HCl, in case of the both uninhibited and inhibited states, with different concentration of ZnO NPs. The Bode diagrams demonstrate an increase in the absolute impedance at low frequencies, confirming that the mitigation of corrosion is better at higher concentration of ZnO NPs. On the other hand, Fig. 7b illustrates a single-phase curve in the central frequency range. This indicates the presence of a unique constant, which is associated with the electrical double layer [44].

Table 3 presents the EIS data for X60 API 5L steel in a 1M HCl corrosive solution for both uninhibited and inhibited ZnO NPs with various concentrations at 298K. The measurements of C_{dl} revealed a decrease in values as the concentration of ZnO NPs increased. This decrease can be attributed to the displacement of water molecules due to NP adsorption, which leads to the formation of a protective barrier film. Consequently, inhibition efficiency is enhanced, which results in a slowdown of the corrosion process. These findings align with the results of polarization tests, which demonstrated a parallel increase in inhibition effectiveness with increasing ZnO NPs concentration, reaching an optimum efficiency of 93.66 % at a concentration of 100 mg/L.

Several studies have explored the use of ZnO NPs as corrosion inhibitors for protecting carbon steel. For instance, Yong et al. investigated ZnO as a corrosion inhibitor in magnesium ammonium phosphate cement (MAPC) coatings. Their study aimed to enhance the anticorrosive performance of MAPC coatings by incorporating varying amounts of ZnO and applying this modified coating to Q235 steel, which was then immersed in a 3.5 % NaCl solution for 28 days. They reported a significantly higher polarization resistance for the ZnO-modified coating, which was 78 % greater efficiency compared to the unmodified coating [45]. In another study, Al-Senani et al. reported the synthesis of ZnO nanoparticles using an extract from Convolvulus arvensis leaves and utilized in corrosion inhibition of carbon steel in a 1 M HCl solution. They evaluated the efficiency using the weight loss method, which revealed an increase with ZnO nanoparticle concentration, peaking at approximately 91 % for 120 mg/L and 90 % for 90 ppm [46]. Similarly, Al-Dahiri et al. investigated the use of Myrrh and ZNO nanoparticles with an average diameter of 75 nm, as corrosion inhibitors for carbon steel in the same 1.0 M HCl solution. The ZnO NPs demonstrated higher inhibition efficiency compared to the Myrrh, achieving up to 89.88 % based on PDP and 92.25 % based on the EIS measurements at 200 mg/L. At a concentration of 100 mg/L, consistent with our study, ZnO NPs exhibited inhibition efficiency of 79.75 % based on the PDP and 87.20 % based on the EIS measurements [47].

Other studies explored the use of both inorganic and organic substances as corrosion inhibitors. For instance, Zhang et al. explored the use of Sb quantum dots (SQDs) containing Sb_2O_4, Sb_2O_3, Sb, and carbon as water-soluble corrosion inhibitors for protecting Q235 steel surfaces in a 0.5 M H_2SO_4 acidic medium. Using electrochemical methods, they observed a corrosion inhibition efficiency of 89.2 % for DPP tests at a concentration of 200 mg/L [48]. This concentration is double than the dose used in the current study, which exhibited lower inhibition efficiency. Most of these concentrations are higher than those used in our study but revealed lower efficiency compared to the results obtained using ZnO nanoparticles synthesized via the NTP, i.e., 93 % efficiency at 100 mg/L. This difference can likely be attributed to the high purity and crystallinity of the ZnO NPs produced via the NTP method, which resulted in small crystallite size and enhanced surface reactivity, and favored superior corrosion protection and inhibition properties [49].

3.2.3. Polarization at 298K–333K

Temperature is an important factor that can simultaneously modify the behavior of inhibitors and substrates in aggressive environments, particularly at high temperatures. As the temperature increases, the inhibitory desorption and rapid dissolution of the formed complexes become more favorable, resulting in a weakening of the corrosion resistance of carbon steel [50,51]. Given this importance, the present study also aims to explore the effect of temperature on the inhibition effectiveness of ZnO NPs for the protection of X60 API 5L steel in a 1M HCl solution. The tests were conducted with a 60 min immersion time using polarization tests and
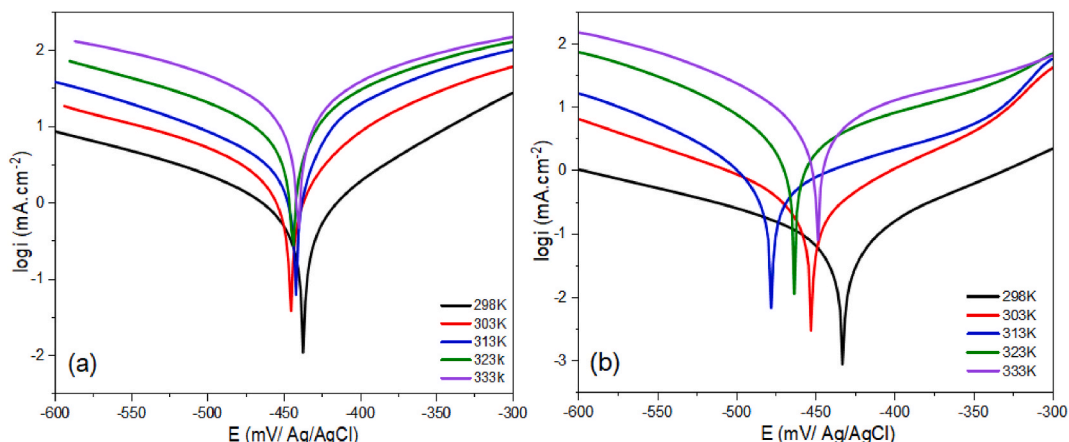
Fig. 8. Polarization curves of X60 API 5L steel uninhibited HCl solution (a) and inhibited with ZnO NPs (b) at varying range of temperatures.

Table 4
Tafel Plots parameters of X60 API-5L steel in 1M HCl uninhibited and containing 100 mg/L ZnO NPs at various temperatures.

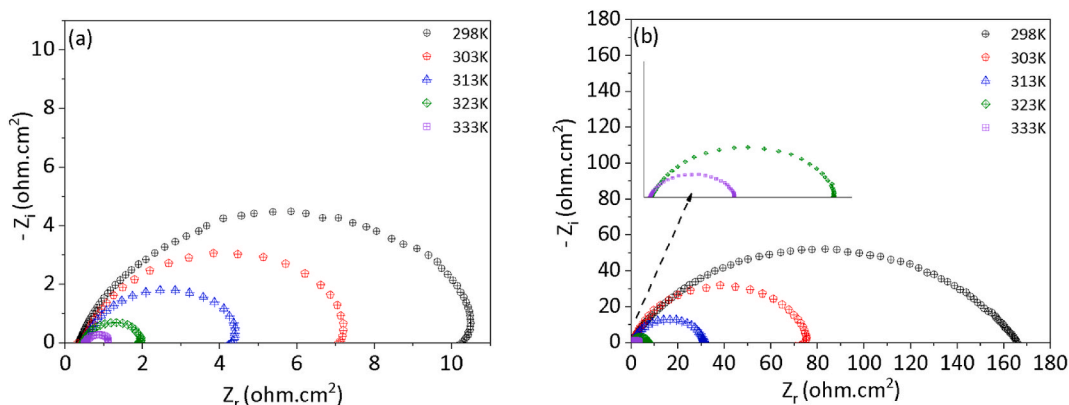| C (mg/L)	Temperature (K)	$-E_{corr}$ (V)	i_{corr} (mA·cm^{-2})	β_a (mV)	$-\beta_c$ (mV)	EI %
Blank	298	436.0	2.4091	82.2	87.7	/
	303	449 0.9	3.6705	98.8	197.2	/
	313	447.6	7.6244	102.2	221.4	/
	323	448.1	11.589	106.6	183.9	/
	333	446.1	26.299	196.6	231.3	/
100 mg/L	298	432.7	0.1564	99.7	89.6	93.50
	303	452.7	0.3675	100.4	118.2	89.98
	313	477.9	1.0698	213.5	106.3	85.96
	323	463.5	3.0232	148.3	83.6	73.91
	333	448.9	9.9482	209.9	108.1	62.17

Fig. 9. EIS Nyquist plots for X60 API 5L steel in 1 M HCl uninhibited (a), and containing 100 mg/L ZnO NPs (b) at various temperatures.

impedance analysis. Both tests were performed without and with the addition of the optimum concentration of 100 mg/L ZnO NPs at temperatures ranging from 298K to 333K. Fig. 8a, b demonstrates that the anodic and cathodic plots exhibit a similar mechanism regarding proton reduction and carbon steel dissolution. The corrosion potential shows a negative shift with increasing temperature in the absence of inhibitors, suggesting an inclination towards accelerated corrosion rates and higher metal dissolution rates at elevated temperatures. However, the presence of ZnO NPs in the HCl solution induces a notable shift towards positive values, even with the rise in temperature, suggesting that the addition of ZnO NPs influences the corrosion potential of X60 API 5L steel.

Table 4 reveals the corrosion behavior of X60 API-5L steel in uninhibited 1M HCl environment and the effect of the inhibitor [52]. The corrosion current density shows an increase in the uninhibited medium, indicating a higher corrosion rate. While, after the addition of 100 mg/L ZnO NPs, a significant decrease in corrosion current density is observed even at higher temperatures. This suggests that ZnO NPs effectively inhibit corrosion. Furthermore, the Tafel slopes in the absence of the inhibitor indicate lower

Table 5
EIS characteristics of X60 API 5L steel in 1M HCl uninhibited and containing 100 mg/L ZnO NPs at various temperatures.

C (mg/L)	Temperature (K)	Rs (ohm·cm^{-2})	Rct (ohm·cm^{-2})	Cdl (mF·cm^{-2})	EI (%)
Blank	298	0.887	10.48	1517	/
	303	0.793	7.019	0.2856	/
	313	0.764	4.114	0.3867	/
	323	0.6607	1.9113	0.2102	/
	333	0.2182	1.13	0.1822	/
100 mg/L	298	0.1957	165.3	0.0684	93.66
	303	0.7465	76.02	0.3233	90.76
	313	0.551	30.91	0.4548	86.69
	323	0.3114	7.56	0.5651	74.71
	333	0.2324	3.01	0.6144	62.45
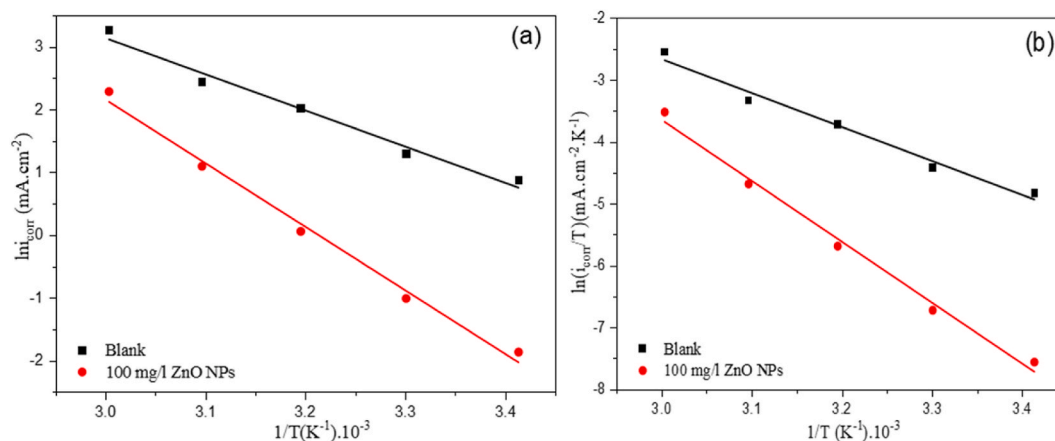
Fig. 10. (a) Arrhenius diagrams of X60 API 5L steel in 1M HCl uninhibited and containing 100 mg/L ZnO NPs at various temperatures (b) Plots of transition states of X60 API 5L steel in 1M HCl uninhibited and containing 100 mg/L ZnO NPs at various temperatures.

polarization resistance, suggesting faster corrosion kinetics. However, after incorporating ZnO NPs, a significant improvement in the corrosion protection is observed. Although the inhibition efficiency of ZnO NPs shows a minor decrease with increasing temperature, these results highlight the effectiveness of ZnO NPs in protecting X60 API 5L steel in 1M HCl acidic environments at elevated temperatures [53].

3.2.4. EIS at 298k—333K

Fig. 9a, b depicts the EIS Nyquist plots for X60 API 5L after immersion in 1M blank HCl solution and an inhibited solution with 100 mg/L ZnO NPs for 60 min of immersion time, at temperatures varying between 298 and 333K. The EIS characteristics for the corrosion of X60 API 5L steel in 1M HCl, both in the uninhibited solution and containing 100 mg/L ZnO NPs at different temperatures are summarized in Table 5. It is clear that the charge transfer resistance decreases with the rise in temperature for the blank solution, suggesting higher corrosion susceptibility. However, R_{ct} increases after the addition of ZnO NPs, while the C_{dl} decreases for each temperature. Additionally, it is observed that R_{ct} decreases as a function of temperature, consequently leading to a slower rate of inhibition. This can be explained by the desorption of the inhibitor's molecules from the X60 API 5L steel surface. In conclusion, the addition of ZnO NPs provided effective corrosion protection at elevated temperatures, demonstrating their potential as a corrosion inhibitor for X60 API 5L steel in 1M HCl acidic media. These findings align with those found previously by potentiodynamic polarization.

3.2.5. Activation energy

The activation energy was examined to assess the impact of temperature on the corrosion of X60 API 5L steel in a blank 1M HCl medium and inhibited with ZnO NPs. The corrosion rate demonstrated a significant dependence on temperature, following an Arrhenius-type behavior of first-order kinetics. These findings were utilized to compute the activation energy via equation (6) [54]:

$$E_a = -(RT/2.303) \ x \ \ln \ (i_{corr}/k) \tag{6}$$

Where, R is the gas constant (8.314 J mol^{-1} K^{-1}), T represents the absolute temperature in Kelvin (0 °C = 273K), i_{corr} is the corrosion current density (A. cm^{-2}), K is the pre-exponential factor of the Arrhenius type, and E_a is the apparent activation energy (J.mol^{-1}). The slopes of the Arrhenius equation were used to determine the thermodynamic parameters for X60 API 5L steel in a blank 1M HCl solution and inhibited with ZnO NPs. An alternative formulation known as the equation of transition state was employed to calculate

Table 6

Thermodynamic behavior of X60 API 5L steel in 1M HCl uninhibited and containing 100 mg/L ZnO NPs at various temperatures.

	E_a (KJ.mol^{-1})	ΔH_a (KJ.mol^{-1})	ΔS_a (J.mol^{-1}. K^{-1})
Blank	47.94	45.63	−83.05
Inhibited	84.23	81.92	−32.25

ΔH_a and ΔS_a following equation (7) [54]:

$$Icorr = (RT / Nxh) \text{ x Exp} (-\Delta Ha / RT) \text{ x Exp} (\Delta Sa / R) \tag{7}$$

Where ΔS_a and ΔH_a represent the activation entropy and enthalpy, respectively. N represents the number of Avogadro, and h represents the plank constant. Fig. 10 depicts the Arrhenius curves at different temperatures (298–333K). The thermodynamic parameters were calculated by extrapolating K_{ads} and E_a from Fig. 10b and regrouped in Table 6.

Table 6 presents the thermodynamic behavior of X60 API 5L steel in a 1M HCl blank solution and an inhibited solution. The results revealed that the addition of 100 mg/L ZnO NPs significantly increased the activation energy E_a from 47.94 to 84.23 kJ mol^{-1}, suggesting that the energy barrier of API 5L X60 steel corrosion reaction increased after adding the inhibitor. This augmentation in the corrosion rate without influencing the inhibition rate process can be attributed to the relative physisorption behavior through electrostatic interactions between the adsorbed ZnO NPs inhibitor and the X60 API 5L steel surface. The higher activation energy values can also be ascribed to the augmentation of double layer thickness [55]. The positive value of the activation enthalpy ΔH_a (81.92 k J mol^{-1}) is greater than that found in the uninhibited solution (45.63 k J mol^{-1}), reflecting the spontaneous and endothermic nature of the X60 API 5L steel dissolution processes. The negative activation entropy ΔS_a values (−83.05 and −32.25 J mol^{-1} K^{-1}) indicate a decrease in disorder or heterogeneity during the corrosion process with the presence of ZnO NPs, potentially reducing the degree of disorder due to the substitution of the water molecules desorbed from the metal surface by the inhibitor molecules [56,57]. These results confirm that ZnO NPs are efficient corrosion inhibitors for X60 API 5L steel in a 1M HCl environment.

3.3. Adsorption isotherm

The interaction between X60 API 5L steel and ZnO NPs molecules can be effectively examined using adsorption isotherms. Various adsorption isotherm models, such as Langmuir, Freundlich, Temkin, and Frumkin, were examined at a temperature of 298K to investigate the adsorption mechanism of ZnO NPs on the carbon steel surface.

The Langmuir isotherm assumes monolayer adsorption of inhibitor molecules onto specific sites on the metal surface. Where each site can hold only one inhibitor molecule without interactions between adsorbed molecules. The Langmuir equation (equation (8)) can be expressed as follow [58]:

$$\theta / (1 - \theta) = Kc \tag{8}$$

Where "K" is the Langmuir adsorption constant, "C" is the inhibitor concentration in the bulk aggressive media, and "θ" is the fraction of the surface covered by the inhibitor, and "m" is the slope of the C_{inh}/θ Vs C. The Langmuir equation can be explained in linear form using equation (9) as follows [58]:

$$C_{inh} / \theta = 1/K + mc \tag{9}$$

On the other hand, the Freundlich isotherm describes multilayer adsorption of the tested inhibitor onto the steel surface, and it can be expressed by equation (10) as follows [59]:

$$\theta = K_f . C_{inh}^{\frac{1}{n}} \tag{10}$$

Where K_f represents the Freundlich equilibrium constant, C is the inhibitor concentration, θ is the surface coverage, and 1/n reflects surface heterogeneity. The Freundlich equation can be explained on linear form using equation (11) as follows [60]:

$$log\ \theta = \log K_f + 1 / n\ (log\ C_{inh}) \tag{11}$$

The Temkin isotherm considers the enthalpy change due to inhibitor interactions. Where all molecules in the layer decrease linearly with coverage due to inhibitor-inhibitor interactions, and can be explained by equation (12) as follows [61]:

$$\theta = \frac{RT}{b} ln\ (K.C_{inh}) \tag{12}$$

Where θ is the surface coverage, b is the adsorption potential, R is the gas constant, T is the Temperature, and K is the equilibrium constant. The Temkin equation can be explained on linear form using equation (13) as follows [61]:

$$\theta = \frac{RT}{b} ln(K) + \frac{RT}{b} ln(C_{inh}) \tag{13}$$

The Frumkin isotherm includes an interaction parameter to account for attractions or repulsions between adsorbed inhibitor
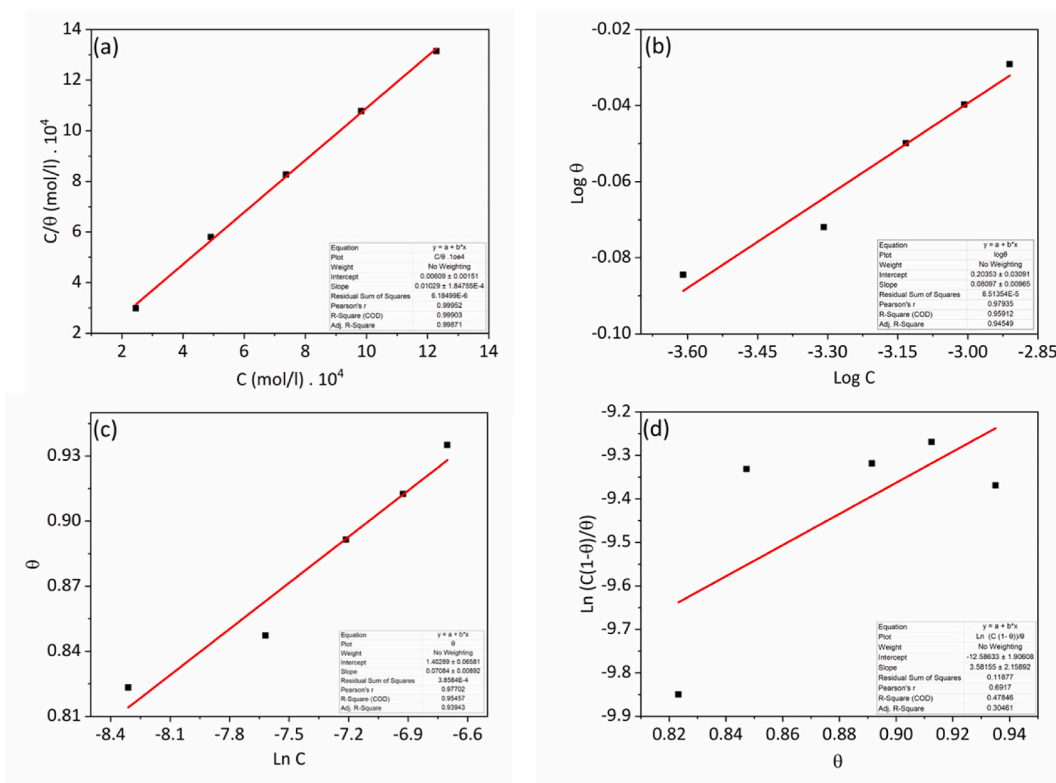
Fig. 11. Adsorption isotherms (a) Langmuir, (b) Freundlish, (c) Temkin, and (d) Frumkin for X60 API 5L steel in 1M HCl inhibited with 100 mg/L ZnO NPs at 298K.

molecules. This can be expressed by equation (14) as follows [62]:

$$\frac{\theta}{(1-\theta)} exp(-2a\theta) = KC_{inh} \tag{14}$$

Where C_{inh} is the inhibitor concentration, θ is the surface coverage, K_{ads} is the equilibrium constant, and a is the interaction parameter. The Frumkin equation can be explained on linear form using equation (15) as follows [62]:

$$\ln\left(\frac{\theta}{1-\theta}\right) = \ln(K_{ads}) + 2a\theta \tag{15}$$

Testing these isotherms is crucial for understanding the adsorption mechanisms, the interaction between the inhibitor and the metal surface, and identifying the most appropriate model. All the tested isotherms (i.e., Langmuir, Freundlish, Temkin, and Frumkin) were plotted, as shown in Fig. 11a–d respectively, and fitted to determine the most suitable isotherm for X60 API 5L steel inhibition in 1M HCl at 298K. The Langmuir adsorption model was found to be the most suitable for the optimum concentration of 100 mg/L, exhibiting a high linear regression coefficient ($R^2 = 0.99$). The Langmuir adsorption isotherm was constructed using (C_{inh}/θ) as a function of C_{inh}. The recovery rates (θ) were obtained from polarization curves, which were determined for various concentrations of ZnO NPs in the aggressive 1M HCl medium at a temperature of 298K as expressed by equation (9) [58].

The thermodynamic parameters were plotted using the Langmuir adsorption isotherm (C_{inh}/θ) as a function of C_{inh} to extrapolate the value of K_{ads}, which was determined to be 1.64×10^4 M^{-1}. This value is directly related to the ΔG_{ads} adsorption standard free enthalpy, expressed by equation (16) as follows [58]:

$$\Delta G_{ads} = -RT \ln(K_{ads} \, C_{H2O}) \tag{16}$$

Where, ΔG_{ads} represents the standard free energy of adsorption. R (8.314 J mol K^{-1}) is denoted as the value of the universal gas constant, T is the room temperature in Kelvin (298K), and C_{H2O} represents the concentration of solvent in this case water ($C_{H2O} = 55.55$ mol l^{-1}) in the solution [62].

The calculated ΔG_{ads} value of -33.99 kJ/mol obtained for the interaction between X60 API 5L steel and ZnO NPs molecules in a corrosive medium of 1M HCl indicates a favorable adsorption process. The negative value suggests that the adsorption is spontaneous and thermodynamically favorable. This finding implies that the ZnO NPs molecules have a strong affinity for the surface of X60 API 5L steel in an acidic environment. This affinity leads to the creation of a protective barrier film on the carbon steel surface, effectively
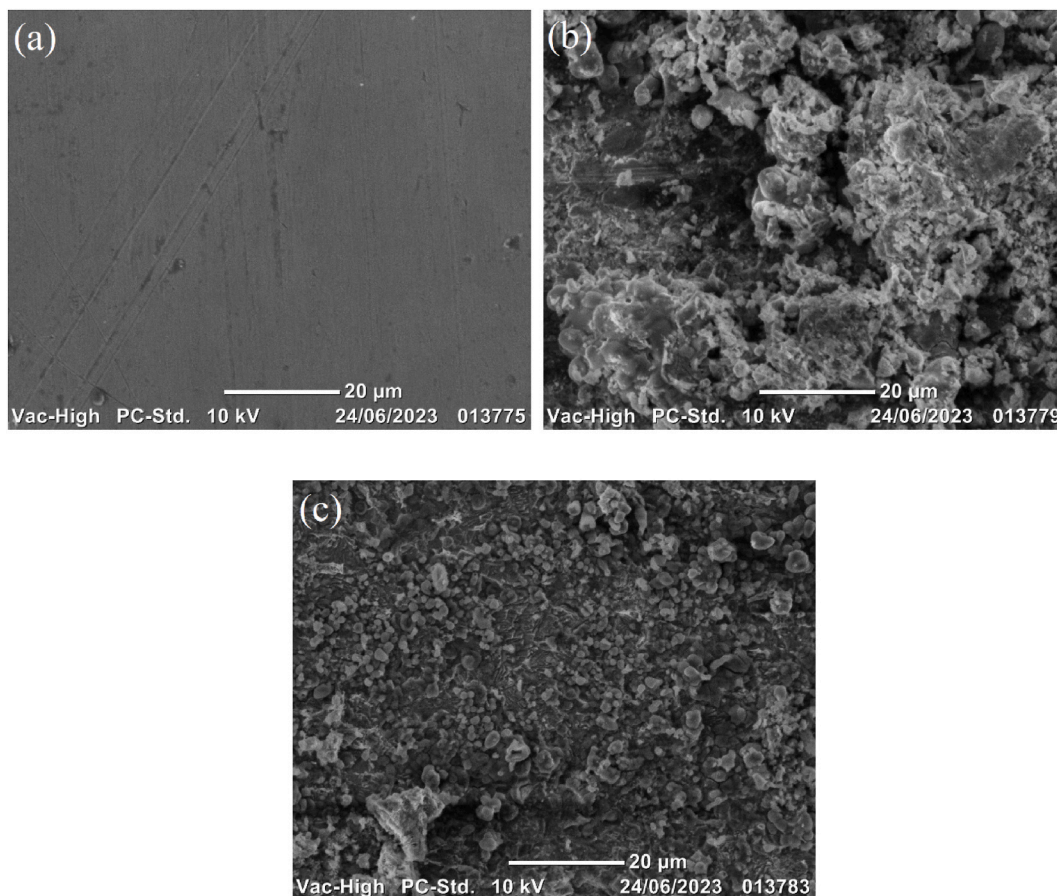
Fig. 12. FE-SEM morphologies of X60 API 5L steel after immersing in 1M HCl (a) nude surface, (b) uninhibited and (b) inhibited with ZnO NPs at 298 K.

retarding corrosion and inhibiting metal dissolution. These observations suggest that the adsorption of ZnO NPs on the steel surface is primarily of a physical nature.

3.4. Surface characterization using FE-SEM and AFM analysis

Field emission scanning electron microscopy (FE-SEM) and atomic force microscopy (AFM) were employed to examine the surface characteristics of the X60 API 5L steel. Their purpose was to provide visual representations of the film formed on the metal surface and the topological changes resulting from exposure to corrosive environments, as well as the subsequent formation of a protective film. The objective was to observe the alterations in the corrosion process by comparing the polished steel, uninhibited and inhibited carbon steel specimens treated with the optimum concentration of ZnO NPs with FE-SEM and AFM. Fig. 12a–c presents the FE-SEM surface morphology of X60 API 5L steel in both nude and immersed conditions for 24 h in a 1M HCl solution, with and without 100 mg/L ZnO NPs corrosion inhibitor. The polished substrate surface exhibited scratch lines that occurred during the polishing process, while the uninhibited corrosive solution resulted in an irregular, pitted, and severely corroded surface. In the case of the inhibited aggressive solution, the surface displayed a more homogenous, smooth surface with fewer pits owing to the formation of a protective layer of the inhibitor on the substrate surface [63,64]. AFM analysis including 3D and 2D topographies confirmed these observations, showing an average surface roughness of 153.01 for the polished specimen (Fig. 13a and b), increasing to 341.19 nm in the untreated corrosive solution of 1M HCl, exhibiting an irregular and pronouncedly corroded surface (Fig. 13c and d) due to rapid metal dissolution in the corrosive solution, and reducing to 186.32 nm in the inhibited solution (Fig. 13e and f) due to the formed protective layer of ZnO NPs [65]. This significant reduction in root Mean Square roughness (RMS) from 341.19 nm to 186.32 nm confirms that ZnO NP is an efficient corrosion inhibitor for X60 API 5L steel in a 1M HCl corrosive medium.

These findings, supported by FE-SEM, AFM, and electrochemical studies, highlight the potential usage of ZnO NPs for corrosion inhibition of X60 API 5L steel in a 1M HCl environment. The corrosion mitigation mechanism is attributed to the adsorption of these nanoparticles onto the steel surface, which forms a protective barrier. Where, the primary mechanism involves the physical adsorption of ZnO NPs onto the steel surface, as indicated by the negative values of ΔG_{ads}, which suggest a spontaneous and thermodynamically favorable adsorption process. This adsorption creates a film that hinders the active sites on the steel surface, effectively blocking these
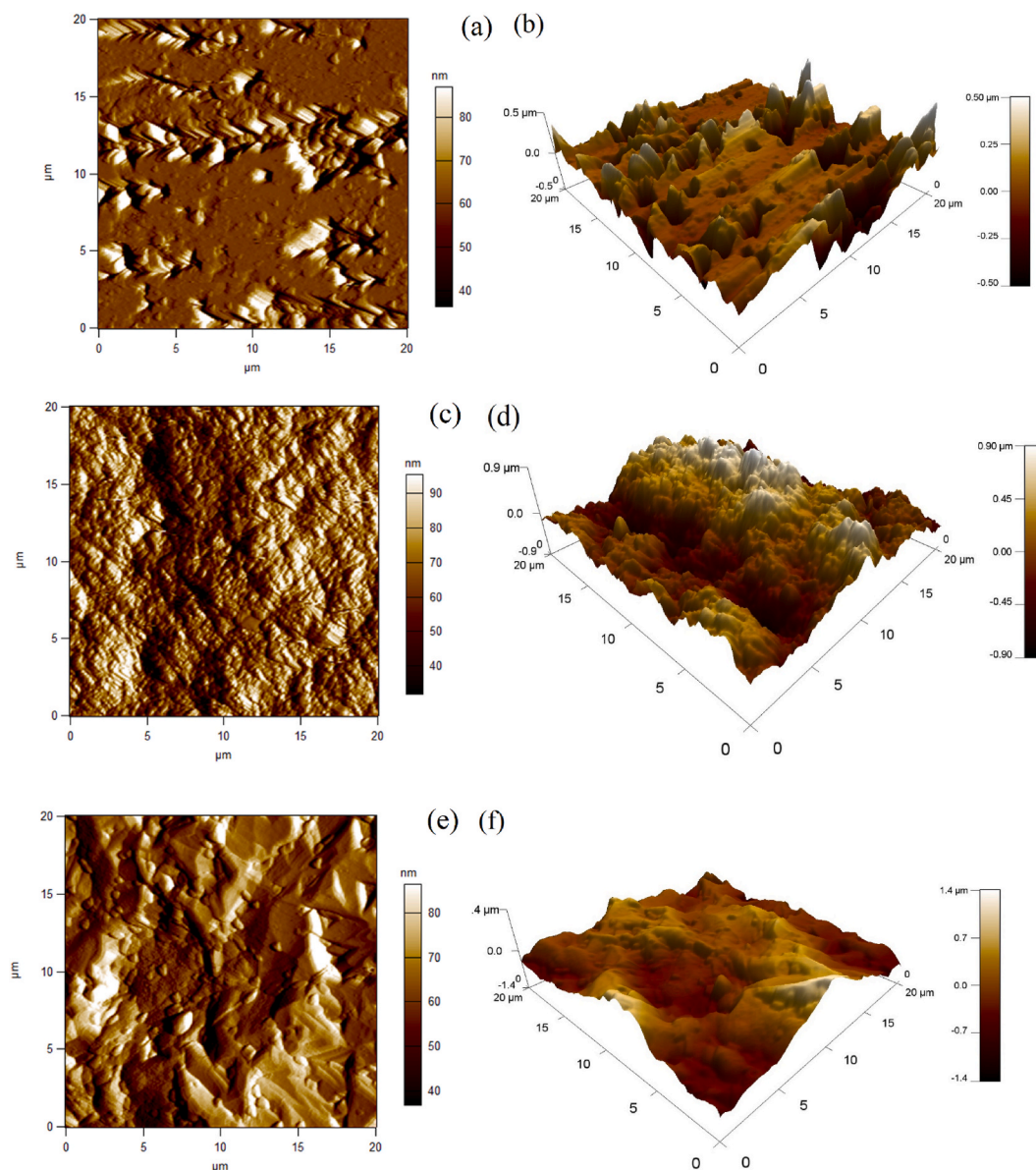
Fig. 13. AFM topographies of X60 API 5L steel after immersing in 1M HCl (a, b) nude surface, (c, d) uninhibited and (e, f) inhibited with ZnO NPs at 298 K.

sites from corrosive species such as H⁺ and Cl⁻ ions, thereby reducing both anodic metal dissolution and cathodic hydrogen evolution reactions [66]. Additionally, ZnO NPs act as a mixed-type inhibitor, impacting both anodic and cathodic reactions. Anodic inhibition occurs as ZnO NPs block anodic sites, reducing the dissolution rate of iron (Fe) into ferrous ions (Fe^{2+}). Cathodic inhibition is achieved by impeding hydrogen ion (H⁺) access to the steel surface, thereby slowing down hydrogen evolution [67]. The increase in the diameter of the Nyquist plots in the EIS analysis with higher ZnO NPs concentrations further supports the formation of a stable and effective protective layer that enhances resistance to corrosion. This protective film mitigates corrosive attack by forming a physical barrier that retards the mass transport of corrosive species to the metal surface, leading to a significant reduction in corrosion current density and an improvement in surface coverage and inhibition efficiency. The ability of ZnO NPs to form a consistent and adherent film on the steel surface, as evidenced by FE-SEM and AFM analyses, further validates their role as a highly effective corrosion inhibitor for X60 API 5L carbon steel in a 1M HCl aggressive solution.

4. Conclusion

The assessment of the inhibitory properties of ZnO nanoparticles synthesized using NTP-GAD on an X60 5L API in a corrosive 1M

HCl environment using various characterization techniques. XRD revealed the hexagonal wurtzite structure and a particle size of 24.41 nm, EDX spectra verified the formation of ZnO NPs, with element weight percentages of oxygen and zinc in the as-prepared ZnO NPs of 27.29 and 72.71 %, and XPS analysis confirmed that zinc is predominantly in the Zn^{2+} oxidation state and oxygen is in the form of the oxide O^{2-}. ZnO NPs demonstrated excellent optical and electronic properties, with a wide band gap of 3.29 eV, as shown in the Tauc plot. Electrochemical impedance spectroscopy revealed a significant corrosion inhibition efficiency of 93.66 % at 100 mg/L, indicating a strong physical adsorption of ZnO NPs onto the steel surface, validated by a negative ΔG_{ads} value (-33.99 kJ/mol) and the increased activation energy (E_a) in the presence of ZnO NPs. Furthermore, the study of the carbon steel surface morphology in a 1M HCl uninhibited solution and inhibited with 100 mg/L of ZnO NPs using FE-SEM and AFM analysis confirms the formation of a uniform protective layer on the X60 API 5L surface. These findings demonstrated that ZnO NPs synthesized through the NTP-GAD method is a strong corrosion inhibitor for X60 API 5L steel in a 1M HCl environment.

Author's contributions

We confirm that all listed authors have made a significant scientific contribution to the research in the manuscript, approved its claims, and agreed to be the authors of this manuscript.

We declare that no further changes to authorship will be made after this point.

Data availability statement

Data will be made available on request.

CRediT authorship contribution statement

Nourelhouda Bounedjar: Writing – original draft, Methodology, Formal analysis, Data curation. **Mohammed Fouad Ferhat:** Writing – original draft, Supervision, Investigation, Funding acquisition, Formal analysis, Data curation, Conceptualization. **Chun Ouyang:** Writing – review & editing, Formal analysis, Data curation. **Mohamed Bououdina:** Writing – review & editing, Resources, Investigation, Conceptualization. **Ihab Shawish:** Writing – review & editing, Formal analysis. **Rasha A. Abumousa:** Writing – review & editing, Funding acquisition, Formal analysis. **Muhammad Humayun:** Writing – review & editing, Supervision, Investigation, Conceptualization.

Declaration of competing interest

The authors declare that they have no known competing financial interests or personal relationships that could have appeared to influence the work reported in this paper.

Acknowledgments

References

[1] G. Wang, Q. Cheng, W. Zhao, Q. Liao, H. Zhang, Review on the transport capacity management of oil and gas pipeline network: challenges and opportunities of future pipeline transport, Energy Strategy Rev. 43 (2022) 100933.

[2] M. Askari, M. Aliofkhazraei, S. Afroukhteh, A comprehensive review on internal corrosion and cracking of oil and gas pipelines, J. Nat. Gas Sci. Eng. 71 (2019) 102971.

[3] I.A.W. Ma, S. Ammar, S.S.A. Kumar, K. Ramesh, S. Ramesh, A concise review on corrosion inhibitors: types, mechanisms and electrochemical evaluation studies, J. Coating Technol. Res. 19 (2022) 241–268.

[4] J. Mohammed Zayan, A.K. Rasheed, A. John, M. Khalid, A.F. Ismail, A. Aabid, M. Baig, Investigation on rheological properties of water-based novel ternary hybrid nanofluids using experimental and taguchi method, Materials 15 (2022) 28.

[5] T.B. Rawal, A. Ozcan, S.-H. Liu, S.V. Pingali, O. Akbilgic, L. Tetard, H. O'Neill, S. Santra, L. Petridis, Interaction of zinc oxide nanoparticles with water: implications for catalytic activity, ACS Appl. Nano Mater. 2 (2019) 4257–4266.

[6] M.U. Aslam Khan, S.I. Abd Razak, W.S. Al Arjan, S. Nazir, T.J. Sahaya Anand, H. Mehboob, R. Amin, Recent advances in biopolymeric composite materials for tissue engineering and regenerative medicines: a review, Molecules 26 (2021) 619.

[7] X.-Q. Zhou, Z. Hayat, D.-D. Zhang, M.-Y. Li, S. Hu, Q. Wu, Y.-F. Cao, Y. Yuan, Zinc oxide nanoparticles: synthesis, characterization, modification, and applications in food and agriculture, Processes 11 (2023) 1193.

[8] F. Chiter, D. Costa, V. Maurice, P. Marcus, Corrosion inhibition of locally de-passivated surfaces by DFT study of 2-mercaptobenzothiazole on copper, npj Mater. Degrad. 5 (2021) 52.

[9] S. Subhasree, P. Anitha, K. Kannan, A. Ramachandran, J.J. Sheri, R. Jayavel, Anticorrosion behavior of ZnO nanoparticles coated on mild steel in NaCl solution, J. Nanosci. Nanotechnol. 20 (2020) 4061–4068.

[10] J. Mohammed Zayan, A.K. Rasheed, A. John, W.F. Faris, A. Aabid, M. Baig, B. Alallam, Synthesis and characterization of novel ternary-hybrid nanoparticles as thermal additives, Materials 16 (2023) 173.

[11] R.A. AbuMousa, U. Baig, M.A. Gondal, M.A. Dastageer, M.S. AlSalhi, B. Moftah, F. Yahya Alqahtani, S. Akhter, F. Sfouq Aleanizy, Investigation of the survival viability of cervical cancer cells (HeLa) under visible light induced photo-catalysis with facile synthesized WO3/ZnO nanocomposite, Saudi J. Biol. Sci. 27 (2020) 1743–1752.

[12] N. Bounedjar, M.F. Ferhat, L. Toukal, R. Messai, Non thermal plasma synthesis of ZnO nanoparticles and their corrosion inhibition activity on XC70 mild steel pipeline in 1 M HCl acidic medium, Mater. Chem. Phys. 311 (2024) 128555.

[13] K. Raju, V. Prasad, R.M. Elavarasan, U. Subramaniam, D.J. Almakhles, Development of high gradient ZnO arrester material for high voltage applications, IEEE Access 8 (2020) 115685–115693.

[14] M. Bouloudenine, H. Laala-Bouali, K. Djeddou, M. Bououdina, N. Grara, Chemical route manufactured ZnO nanoparticles and their biological accumulation, J. Inorg. Organomet. Polym. Mater. 32 (2022) 1966–1974.

[15] J.N. Hasnidawani, H.N. Azlina, H. Norita, N.N. Bonnia, S. Ratim, E.S. Ali, Synthesis of ZnO nanostructures using sol-gel method, Procedia Chem. 19 (2016) 211–216.

[16] C.M. Montemayor Palos, A.E. Mariño-Gámez, G.-E. Acosta-González, M.B. Hernández, S. García-Villarreal, L. Falcon Franco, L. García-Ortiz, J.A. Aguilar-Martínez, Large-scale production of ZnO nanoparticles by high energy ball milling, Phys. B Condens. Matter 656 (2023) 414776.

[17] T. Song, R. Li, J. Wang, C. Dong, X. Feng, Y. Ning, R. Mu, Q. Fu, Enhanced methanol synthesis over self-limited ZnO overlayers on Cu nanoparticles formed via gas-phase migration route, Angew. Chem. Int. Ed. 63 (2024) e202316888.

[18] M. Hosni, S. Farhat, F. Schoenstein, F. Karmous, N. Jouini, B. Viana, A. Mgaidi, Ultrasound assisted synthesis of nanocrystalline zinc oxide: experiments and modelling, J. Alloys Compd. 615 (2014) S472–S475.

[19] R. Müller, F. Huber, O. Gelme, M. Madel, J.-P. Scholz, A. Minkow, U. Herr, K. Thonke, Chemical vapor deposition growth of zinc oxide on sapphire with methane: initial crystal formation process, Cryst. Growth Des. 19 (2019) 4964–4969.

[20] A. Pruna, I. Poliac, D. Busquets Mataix, A. Ruotolo, Synergistic effects in ZnO nanorod films by pulsed electrodeposition on graphene oxide towards enhanced photocatalytic degradation, Ceram. Int. 50 (2024) 4622–4631.

[21] L. Benkhira, M.F. Ferhat, M.T.O. Khaled, R. Messai, N. Bounedjar, M.L. Tedjani, A. Zoukel, M. Humayun, M. Bououdina, Multifunctional assessment of copper-doped ZnO nanoparticles synthesized via gliding arc discharge plasma technique: antioxidant, antibacterial, and photocatalytic performance, Environ. Sci. Pollut. Control Ser. 31 (2024) 43743–43756.

[22] R. Aboorvakani, S.J. Kennady Vethanathan, K.U. Madhu, Influence of Zn concentration on zinc oxide nanoparticles and their anti-corrosion property, J. Alloys Compd. 834 (2020) 155078.

[23] B.J. Usman, S.A. Umoren, Z.M. Gasem, Inhibition of API 5L X60 steel corrosion in CO2-saturated 3.5% NaCl solution by tannic acid and synergistic effect of KI additive, J. Mol. Liq. 237 (2017) 146–156.

[24] A. Tiya-Djowe, S. Laminsi, G.L. Noupeyi, E.M. Gaigneaux, Non-thermal plasma synthesis of sea-urchin like α-FeOOH for the catalytic oxidation of Orange II in aqueous solution, Appl. Catal. B Environ. 176–177 (2015) 99–106.

[25] R. Messai, M.F. Ferhat, B. Belmekki, M.W. Alam, M.A.S. Al-Othoum, S. Sadaf, GAD plasma-assisted synthesis of ZnO nanoparticles and their photocatalytic activity, Mater. Res. Express 11 (2024) 015006.

[26] C.M. Anbarasi, S. Rajendran, Surface protection of carbon steel by hexanesulphonic acid-zinc ion system, Int. Sch. Res. Notices 2014 (2014) 628604.

[27] V. Dhiman, N. Kondal, Prashant, Bryophyllum pinnatum leaf extract mediated ZnO nanoparticles with prodigious potential for solar driven photocatalytic degradation of industrial contaminants, Environ. Res. 216 (2023) 114751.

[28] C.F. Holder, R.E. Schaak, Tutorial on powder X-ray diffraction for characterizing nanoscale materials, ACS Nano 13 (2019) 7359–7365.

[29] A. Kumar, Z.A. Ansari, H. Fouad, A. Umar, S.G. Ansari, Oxidative stress control in E. coli and S. aureus cells using amines adsorbed ZnO, Sci. Adv. Mater. 6 (2014) 1236–1243.

[30] S.P. Rajendran, K. Sengodan, Synthesis and characterization of zinc oxide and iron oxide nanoparticles using Sesbania grandiflora leaf extract as reducing agent, Journal of Nanoscience 2017 (2017) 8348507.

[31] K. Davis, R. Yarbrough, M. Froeschle, J. White, H. Rathnayake, Band gap engineered zinc oxide nanostructures via a sol–gel synthesis of solvent driven shape-controlled crystal growth, RSC Adv. 9 (2019) 14638–14648.

[32] M.L. da Silva-Neto, M.C.A. de Oliveira, C.T. Dominguez, R.E.M. Lins, N. Rakov, C.B. de Araújo, L.d.S. Menezes, H.P. de Oliveira, A.S.L. Gomes, UV random laser emission from flexible ZnO-Ag-enriched electrospun cellulose acetate fiber matrix, Sci. Rep. 9 (2019) 11765.

[33] M. Ahmad, W. Rehman, M.M. Khan, M.T. Qureshi, A. Gul, S. Haq, R. Ullah, A. Rab, F. Menaa, Phytogenic fabrication of ZnO and gold decorated ZnO nanoparticles for photocatalytic degradation of Rhodamine B, J. Environ. Chem. Eng. 9 (2021) 104725.

[34] I. Saleem, N.F. Rana, T. Tanweer, W. Arif, I. Shafique, A.S. Alotaibi, H.A. Almukhlifi, S.A. Alshareef, F. Menaa, Effectiveness of Se/ZnO NPs in enhancing the antibacterial activity of resin-based dental composites, Materials 15 (2022) 7827.

[35] Y. Miao, A. Yokochi, G. Jovanovic, S. Zhang, A. von Jouanne, Application-oriented non-thermal plasma in chemical reaction engineering: a review, Green Energy and Resources 1 (2023) 100004.

[36] A. Hossain, Y. Abdallah, M.A. Ali, M.M. Masum, B. Li, G. Sun, Y. Meng, Y. Wang, Q. An, Lemon-fruit-based green synthesis of zinc oxide nanoparticles and titanium dioxide nanoparticles against soft rot bacterial pathogen dickeya dadantii, Biomolecules 9 (2019) 863.

[37] G. Qu, G. Fan, M. Zhou, X. Rong, T. Li, R. Zhang, J. Sun, D. Chen, Graphene-modified ZnO nanostructures for low-temperature NO2 sensing, ACS Omega 4 (2019) 4221–4232.

[38] W. Liu, T. He, Y. Wang, G. Ning, Z. Xu, X. Chen, X. Hu, Y. Wu, Y. Zhao, Synergistic adsorption-photocatalytic degradation effect and norfloxacin mechanism of ZnO/ZnS@BC under UV-light irradiation, Sci. Rep. 10 (2020) 11903.

[39] L. Toukal, M. Foudia, D. Haffar, N. Aliouane, M. Al-Noaimi, Y. Bellal, H. Elmsellem, I. Abdel-Rahman, Monte Carlo simulation and electrochemical performance corrosion inhibition whid benzimidazole derivative for XC48 steel in 0.5 M H2SO4 and 1.0 M HCl solutions, J. Indian Chem. Soc. 99 (2022) 100634.

[40] I.B. Onyeachu, D.S. Chauhan, M.A. Quraishi, I.B. Obot, A. Singh, (E)-2-amino-7-hydroxy-4-styrylquinoline-3-carbonitrile as a novel inhibitor for oil and gas industry: influence of temperature and synergistic agent, J. Adhes. Sci. Technol. 36 (2022) 1858–1882.

[41] N. Sait, N. Aliouane, N. Ait Ahmed, L. Toukal, M. Al-Noaimi, Synergistic effect of potassium iodide on corrosion inhibition of copper by tetraphosphonic acid in hydrochloric acid solution, J. Adhes. Sci. Technol. 36 (2022) 109–133.

[42] L. Mekhiche, N. Maouche, B. Nessark, L. Toukal, H. Ayadi, Composites of polyanine/CdTe for corrosion protection of mild steel XC 70 in a 3.5% NaCl solution, J. Adhes. Sci. Technol. 35 (2021) 2602–2624.

[43] L. Toukal, S. Keraghel, F. Benghanem, A. Ourari, Electrochemical, thermodynamic and quantum chemical studies of synthesized benzimidazole derivative as an eco-friendly corrosion inhibitor for XC52 steel in hydrochloric acid, Int. J. Electrochem. Sci. 13 (2018) 951–974.

[44] B.T. K, J. C, A. P, Corrosion inhibition of mild steel in hydrochloric acid by leaves extract of Tephrosia purpurea, J. Adhes. Sci. Technol. 34 (2020) 2424–2447.

[45] Y. Zhi, Q. Wu, H. Ma, Y. Wu, M. Akbar, X. Zhao, N. Yang, Effect of zinc oxide on corrosion resistance of magnesium ammonium phosphate cement-based coating, Construct. Build. Mater. 398 (2023) 132473.

[46] G.M. Al-Senani, Synthesis of ZnO-NPs using a Convolvulus arvensis leaf extract and proving its efficiency as an inhibitor of carbon steel corrosion, Materials 13 (2020) 890.

[47] R.H. Al-Dahiri, A.M. Turkustani, M.A. Salam, The application of zinc oxide nanoparticles as an eco-friendly inhibitor for steel in acidic solution, Int. J. Electrochem. Sci. 15 (2020) 442–457.

[48] R. Zhang, L. Xiong, Z. He, J. Pu, L. Guo, Synthesis and structure of water-soluble Sb quantum dots and enhanced corrosion inhibition performance and mechanisms, Inorg. Chem. 60 (2021) 16346–16356.

[49] R. Messai, M.F. Ferhat, A. Serouti, B. Nourelhouda, M. Humayun, N. Allag, A. Zoukel, M.R. Ghezzar, M. Bououdina, Rapid synthesis of ZnO nanoparticles via gliding arc discharge: unveiling the impact of discharge time on particle properties and photocatalytic performance, Environ. Sci. Pollut. Control Ser. 31 (2024) 33885–33903.

[50] A.H. Mostafatabar, G. Bahlakeh, M. Ramezanzadeh, B. Ramezanzadeh, Eco-friendly protocol for zinc-doped amorphous carbon-based film construction over steel surface using nature-inspired phytochemicals: coupled experimental and classical atomic/molecular and electronic-level theoretical explorations, J. Environ. Chem. Eng. 9 (2021) 105487.

[51] R. Saidi, K. Raeissi, F. Ashrafizadeh, M. Kharaziha, The effect of zinc oxide coating morphology on corrosion performance of Ti-6Al-4 V alloys, J. Alloys Compd. 883 (2021) 160771.

[52] M.T. Alhaffar, S.A. Umoren, I.B. Obot, S.A. Ali, M.M. Solomon, Studies of the anticorrosion property of a newly synthesized Green isoxazolidine for API 5L X60 steel in acid environment, J. Mater. Res. Technol. 8 (2019) 4399–4416.

[53] Y. Li, Y. Yin, L. Li, Conferring NiTi alloy with controllable antibacterial activity and enhanced corrosion resistance by exploiting Ag@PDA films as a platform through a one-pot construction route, Heliyon 10 (2024) e34154.

[54] I.B. Onyeachu, I.B. Obot, A.H. Alamri, C.A. Eziukwu, Effective acid corrosion inhibitors for X60 steel under turbulent flow condition based on benzimidazoles: electrochemical, theoretical, SEM, ATR-IR and XPS investigations, Eur. Phys. J. Plus (2020) 135, https://doi.org/10.1140/epjp/s13360-020-00167-4.

[55] X. Dayu, L. Mingxing, K.R. Ansari, A. Singh, Synthesis of novel nano polymeric composite of zinc oxide and its application in corrosion inhibition of tubular steel in sweet corrosive medium, J. Mol. Liq. 359 (2022) 119327.

[56] D.S. Chauhan, P. Singh, M.A. Quraishi, Quinoxaline derivatives as efficient corrosion inhibitors: current status, challenges and future perspectives, J. Mol. Liq. 320 (2020) 114387.

[57] O.O. Ogunleye, A.O. Arinkoola, O.A. Eletta, O.O. Agbede, Y.A. Osho, A.F. Morakinyo, J.O. Hamed, Green corrosion inhibition and adsorption characteristics of Luffa cylindrica leaf extract on mild steel in hydrochloric acid environment, Heliyon 6 (2020) e03205.

[58] A. Kokalj, On the use of the Langmuir and other adsorption isotherms in corrosion inhibition, Corrosion Sci. 217 (2023) 111112.

[59] J. Wang, X. Guo, Adsorption isotherm models: classification, physical meaning, application and solving method, Chemosphere 258 (2020) 127279.

[60] O. Abakedi, M. Sunday, M. James, Mild steel corrosion inhibition in acidic medium by Jatropha tanjorensis stem bark extract, Chemical Science International Journal 9 (2021) 9–13.

[61] K.H. Chu, Revisiting the Temkin isotherm: dimensional inconsistency and approximate forms, Ind. Eng. Chem. Res. 60 (2021) 13140–13147.

[62] A. Fouda, H. Abdel-Fatah, N. Abdallah, M. Ahmd, Corrosion inhibition of nickel in HCl solution by some indole derivatives, Int. J. Electrochem. Sci. 8 (2013) 3390–3405.

[63] T. Subramaniam, M.B. Idris, S.K. S, R.K. S, D. S, Mitigating hydrogen evolution reaction and corrosion of zinc in electrically rechargeable zinc-air batteries using nanofluid electrolytes, J. Energy Storage 81 (2024) 110457.

[64] M. Omotioma, O.D. Onukwuli, I.A. Nnanwube, Testing the inhibition efficiency of the castor oil leaf as corrosion inhibitor of mild steel in H2SO4, Heliyon 10 (2024) e31168.

[65] E.B. Aydin, G. Siğircik, H.A.M. Takci, Antimicrobial properties and corrosion behavior of TiO2NTs electrodes modified with Ag and ZnO nanorod in simulated body fluid solution, J. Mol. Struct. 1240 (2021) 130569.

[66] G. Gómez-Sánchez, O. Olivares-Xometl, P. Arellanes-Lozada, N.V. Likhanova, I.V. Lijanova, J. Arriola-Morales, V. Díaz-Jiménez, J. López-Rodríguez, Temperature effect on the corrosion inhibition of carbon steel by polymeric ionic liquids in acid medium, Int. J. Mol. Sci. 24 (2023) 6291.

[67] K. Belal, A.H. El-Askalany, E.A. Ghaith, A. Fathi Salem Molouk, Novel synthesized triazole derivatives as effective corrosion inhibitors for carbon steel in 1M HCl solution: experimental and computational studies, Sci. Rep. 13 (2023) 22180.